Biosensors and Bioelectronics 141 (2019) 111419

Contents lists available at ScienceDirect

Biosensors and Bioelectronics

journal homepage: www.elsevier.com/locate/bios

Terminal deoxynucleotidyl transferase (TdT)-catalyzed homo-nucleotides-constituted ssDNA: Inducing tunable-size nanogap for core-shell plasmonic metal nanostructure and acting as Raman reporters for detection of *Escherichia coli* O157:H7

Yangyang Zhou[a,1], Weina Fang[b,1], Keqiang Lai[a], Yongheng Zhu[a], Xiaojun Bian[a], Jianlei Shen[c], Qian Li[c], Lihua Wang[b], Weijia Zhang[d,**], Juan Yan[a,*]

[a] Laboratory of Quality and Safety Risk Assessment for Aquatic Products on Storage and Preservation (Shanghai), Ministry of Agriculture, Shanghai Engineering Research Center of Aquatic-Product Process & Preservation, College of Food Science and Technology, Shanghai Ocean University, Shanghai, 201306, China
[b] Division of Physical Biology & Bioimaging Center, Shanghai Synchrotron Radiation Facility, Shanghai Institute of Applied Physics, Chinese Academy of Sciences, Shanghai, 201800, China
[c] School of Chemistry and Chemical Engineering, Shanghai Jiao Tong University, Shanghai, 200240, China
[d] Fifth People's Hospital of Shanghai and Institutes of Biomedical Sciences, and State Key Laboratory of Molecular Engineering, Fudan University, Shanghai, 200032, China

ARTICLE INFO

Keywords:
Terminal deoxynucleotidyl transferase (TdT)
Core-shell nanostructures
Nanogap
Surface enhanced Raman spectroscopy (SERS)
Bacterial detection

ABSTRACT

Core-shell plasmonic metal nanoparticles with interior nanogaps are superior nanostructures owing to their large signal enhancement for Surface enhanced Raman spectroscopy (SERS). Herein, we incorporated Terminal deoxynucleotidyl transferase (TdT)-catalyzed DNA in the preparation of core-shell nanostructures for the detection of *Escherichia coli* O157:H7 (*E. coli* O157:H7) cells. The elongated products-homo-nucleotides-composed of long single DNA strands (hn-D) are used not only to induce tunable-size nanogaps but also as Raman reporters with consistent and uniform signal enhancement. Using this synthetic process of hn-D-embedded core-shell nanoparticles (hn-DENPs), we found that the length of hn-D strands affects the size of the nanogap. In addition, performances of the specific Raman imaging of *E. coli* O157:H7, high detection sensitivity of 2 CFU/mL, and the recovery of 98.1%–105.2% measured in the real food samples, make hn-DENP a biosensor that will be widely used in biological detection.

1. Introduction

Surface-enhanced Raman scattering (SERS) is a sensitive analytical technique which can identify the molecular species and provide structural information with sensitivity to single molecular functionalities through their unique vibrational fingerprints (Fleischmann et al., 1974; Graham et al., 2017; Nie and Emory, 1997; Saleh et al., 2017; Stiles et al., 2008). It has been extensively employed in a wide variety of applications such as clinical diagnosis, food safety, and environmental protection (Al-Shalalfeh et al., 2016; Granger et al., 2016; Harper et al., 2013; Kneipp et al., 2008; Laing et al., 2016; Qian et al., 2008; Saleh et al., 2018; Schlucker, 2014; Xie et al., 2018). However, the controllable-distributed "hot spots" and the uniformity of SERS enhancement are still remaining challenges in the SERS measurement (Lim et al., 2011).

Recently, the synthesis plasmonic metal nanostructures (PMNs) especially those of noble core-shell PMNs with interior nanogap have attracted increasing interest owing to their highly stable, reproducible "hot spots" and significant potential in multiplexed biosensing and bioimaging application (Alaqad and Saleh, 2016; Guo et al., 2015; Kang et al., 2015; Li et al., 2017; Lim et al., 2010; Nam et al., 2016). Nam et al. pioneered the field by using short polybase-modified Au nanoparticles (AuNPs) as seeds to synthesize core-shell nanostructures with hollow nanogaps (~1 nm) (Kumar et al., 2016; Lee et al., 2016; Lim et al., 2011; Nam et al., 2016). DNA has been then exploited to control the assembly and growth of core-shell PMNs (Guerrini and Graham, 2012; Hu et al., 2016; Lee et al., 2012; Oh et al., 2014; Shen et al. 2014, 2015). Core-shell PMNs are now strongly pursued also because they

* Corresponding author.
** Corresponding author.
E-mail addresses: weijiazhang@fudan.edu.cn (W. Zhang), j-yan@shou.edu.cn (J. Yan).
[1] these authors contributed equally to this work.

https://doi.org/10.1016/j.bios.2019.111419
Received 1 April 2019; Received in revised form 3 June 2019; Accepted 5 June 2019
Available online 08 June 2019
0956-5663/

provide tunable interior nanogap and localized surface plasmon resonance (LSPR) which is responsible for the electromagnetic enhancement factor in SERS (Li et al., 2017; Nam et al., 2016). However, in their follow-up work, Nam and co-workers varied polybases length and found that the change in DNA length does not have significant effect on the size of interior nanogap (Oh et al., 2014). In fact, other published examples using polymers and small molecules as template to fabricate intra-gap core-shell nanostructures led to different conclusions (Khlebtsov and Khlebtsov, 2016; Saleh et al., 2016; Song et al., 2014; Zhang et al., 2017). For example, different amounts of Raman reporter molecules, embedded in core-shell nanoparticles, modified the size of nanogap (Lin et al. 2017, 2018). Controlling over the polymer thickness inside the nanoparticles (Song et al., 2014) or tuning the thickness of the assembled molecular layers embedded within the core-shell nanostructure (Lin et al., 2017) changes the size of the interior nanogap. However, DNA-based core shell PMNs with tunable nanogaps have been rarely reported.

On the other hand, the existing SERS technology using typical Raman molecules often have defects such as weak fixation on the metal surface, leading to easy elimination and destruction after subsequent washing treatments (Lin et al., 2018). In addition, the limited surface area of the metal surface also affects the number of Raman molecules that linked to its surface by adsorption (Graham et al., 2017).

Here, we report a controllable route to prepare Au@Au core-shell plasmonic nanostructures with built-in nanogaps that are precisely tuned by controlling the immobilization of Terminal deoxynucleotidyl transferase (TdT)-catalyzed homo-nucleotides-composed of long single strands of DNA. The homo-nucleotides consist of adenine or thymine hn-D (hn-D, n = adenine, A or thymine, T) coupled to the surface of Au cores. TdT, a template-independent DNA polymerase, has the ability to catalyze the sequential addition of deoxynucleotides (dNTPs) at the 3′OH group of the deoxyribose to produce a long single-stranded DNA (ssDNA) nanotail (Deng et al., 2019; Wan et al., 2015). In this study, two short strands of DNA: polyA$_{10}$ and polyT$_{10}$ modified with an external thiol group, were immobilized on the surface of Au nanoparticles (AuNPs). After TdT elongation, we obtained hA-D-embedded core-shell nanoparticles (hA-DENPs) and hT-D-embedded core-shell nanoparticles (hT-DENPs), respectively. hT-DENPs were functionalized further with antibody, resulting in hT-D-embedded core-shell SERS tags (hT-DETs,) for the specific detection of *Escherichia coli* O157:H7 (*E. coli* O157:H7). Comparing with previously typical SERS methods, the presence of hn-D strands ensures their stability as Raman reporters because of the linkage of the phosphodiester bond and avoids the extra Raman molecules. Furthermore, the number of Raman reporters on the metal surface is massively improved by TdT amplification. The concept behind this approach is illustrated in Scheme 1.

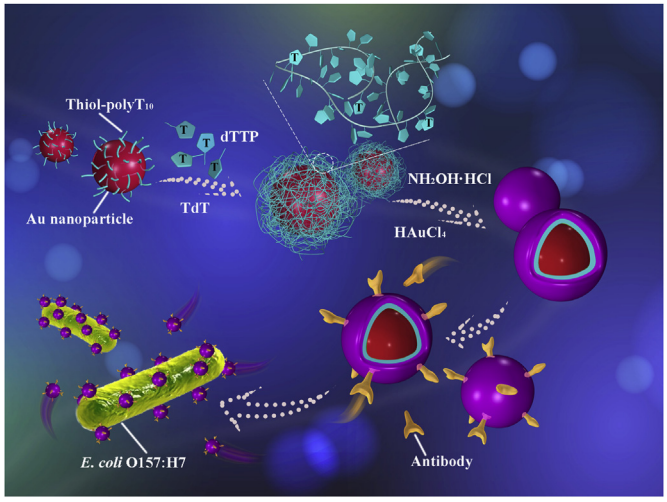

Scheme 1. Schematic illustration of the synthetic sequence in producing hT-DENPs for specific recognition of *E. coli* O157:H7. TdT: Terminal deoxynucleotidyl transferase.

2. Experimental section

Chemicals and Reagents;
Apparatus;
Experimental details;
and Characterizations are available in the Supporting Information.

3. Results and discussion

3.1. TdT elongation on Au surfaces

Thiol-polyA$_{10}$ was initially anchored on the surface of AuNPs (~15 nm diameter) via the Au-SH bond of the Au-polyA$_{10}$. TdT-mediated incorporation of the chain of identical nucleotides (dATP) on the 3′-OH terminals of this nanoconjugate, resulted in an Au-hA-D seed for subsequent core-shell nanostructure. As shown in Fig. S1A, although the color change was not obvious after DNA chain assembly (Au-polyA$_{10}$) and TdT-catalyzed amplification DNA layer (Au-hA-D), it can be seen from the UV-Vis spectrum (Fig. S1B) that the AuNPs first displayed an absorbance peak at 520 nm. The absorbance peak red shifted from 520 to 527 nm, then to 550 nm as the NP surface converted from Au-polyA$_{10}$ to Au-hA-D. Agarose gel electrophoresis and atomic force microscopy (AFM) images were also used to characterize the enzyme-mediated process. Gel images are compared in Fig. 1, showing both AuNPs bands (A) under white light, and DNA bands (B) under UV illumination. As shown in Fig. 1A, both Au-hA-D and Au-hT-D products (lane 1 and lane 2) obtained by TdT-catalyzed elongation on the surface of Au-polyA$_{10}$ and Au-polyT$_{10}$ nanoconjugates (lane 3 and lane 4, respectively) showed marked reduction of electrophoretic mobility. The positions of these AuNPs bands indicated a dramatic increase of molecular weight after TdT elongation. When the same bands were illuminated under UV, however, there were no visible strands of DNA (Fig. 1B, lane 1 through lane 4). That's probably because the DNA strands were too short (lane 3 and lane 4); or composed of only one kind of nucleotide (lane 1 and lane 2), resulting in unsuccessful staining. This explanation is further confirmed by the observation that after hybridization between Au-hA-D and Au-hT-D took place, the hybrid product resulted in a prominent AuNP band and a DNA band very close to the sample well (lane 5, Fig. 1A&B). At the same time, hybridization of the two starting probes (Au-polyA$_{10}$ and Au-polyT$_{10}$) still did not reveal any significant DNA bands (Fig. 1A and B, lane 6). These data indicated that TdT effectively catalyzes the elongation of DNA and we can obtain amplified hn-D chains on the AuNPs surface.

AFM imaging provided further direct evidence for *in situ* TdT elongation on AuNPs. Fig. 1C&D showed the schematic diagrams and the corresponding AFM images of Au-hA-D and Au-hT-D that were composed of the same nucleotide bases, respectively. As detailed in Fig. 1C&D, linear elongated hn-D strands (yellow) were prominently stretched from the surface of AuNPs (white spots). Some of hn-D strands may stick together and condense into globular structure as the flexibility of the sugarphosphate backbones and the electrostatic attraction between each other.

3.2. Synthesis of Au shell based on Au-hn-D seeds

After confirming the elongation of hn-D strands on the surface of AuNPs, we used Au-hn-D as seeds to synthesize a gold shell. The structures of hn-DENPs were confirmed using UV-Vis spectroscopy, high-resolution transmission electron microscopy (HRTEM), and high-Angle Annular Dark Field scanning transmission electron microscopy (HAADF-STEM). As shown in Fig. 1E, as the final Au@Au core-shell nanostructures are formed, the color of the solution changes markedly

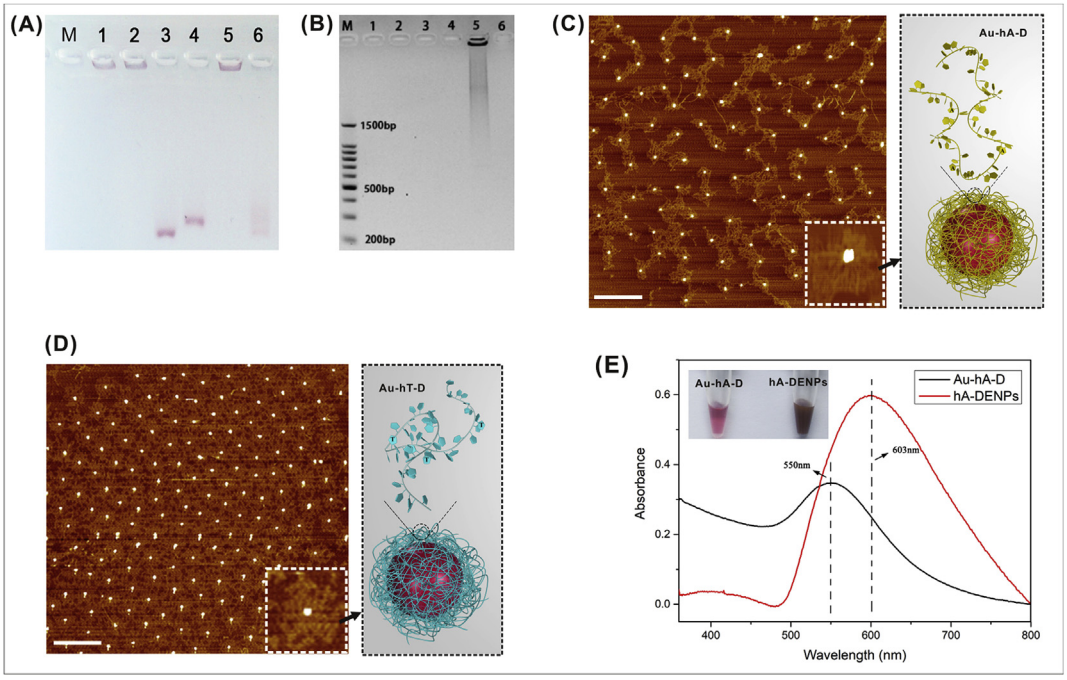

Fig. 1. (A) The gel was imaged under white light. M: 100 bp ladder marker, lane 1: Au-hA-D, lane 2: Au-hT-D, lane 3: Au-polyA$_{10}$, lane 4: Au-polyT$_{10}$, lane 5: hybrid product of 1 and 2, lane 6: hybrid product of 3 and 4. (B) The same gel stained with GelRed was imaged under an ultraviolet lamp. (C) Illustration and AFM image of Au-hA-D. Insert: Individual Au-hA-D. (D) Illustration and AFM image of Au-hT-D. Insert: Individual Au-hT-D. Scale bars were 1 μm and height scales were 10 nm. (E) UV-vis spectra of prepared Au-hA-D and hA-DENPs. Insert: Au-hA-D and hA-DENPs solution. The products used were analyzed with 1.0% (w/v) agarose gel electrophoresis, running in 1 × Tris-acetate-EDTA (TAE) (pH 8.4) at room temperature. Electrophoresis was performed at a constant potential of 110 V for 30 min. All the AFM samples were imaged in a ScanAsyst in air mode under ambient conditions.

(Insert), and the UV-Vis spectrum of the nanoparticles undergoes a prominent red shift from 550 nm (Au-hA-D) to 603 nm (hA-DENPs) with a broader peak shape, which is consistent with our previous studies (Hu et al., 2016).

In the process of synthesizing the Au shell, using Au-hA-D as seeds, we found budding structures (Fig. 2A–i, red arrows), half-shell structures (Fig. 2A–ii, yellow arrows), nearly complete structures (Fig. 2A–iii) and ultimately nanogap-containing core-shell nanostructures (Fig. 2A–iv) were formed. Au-hT-D seeds generated popcorn-like Au shell structures at the early stage of the synthesis (Fig. 2B–i). This indicates that the hn-D strand can mediate the formation of an Au shell, although by using catalyzed TdT elongation, the length of the DNA chain is much longer than that of polybases used in previous reports (Lim et al., 2011; Oh et al., 2014).

3.3. Nanogap formation based on Au-hA-D seeds

We next focused on how the resulting nanogaps were affected by hn-

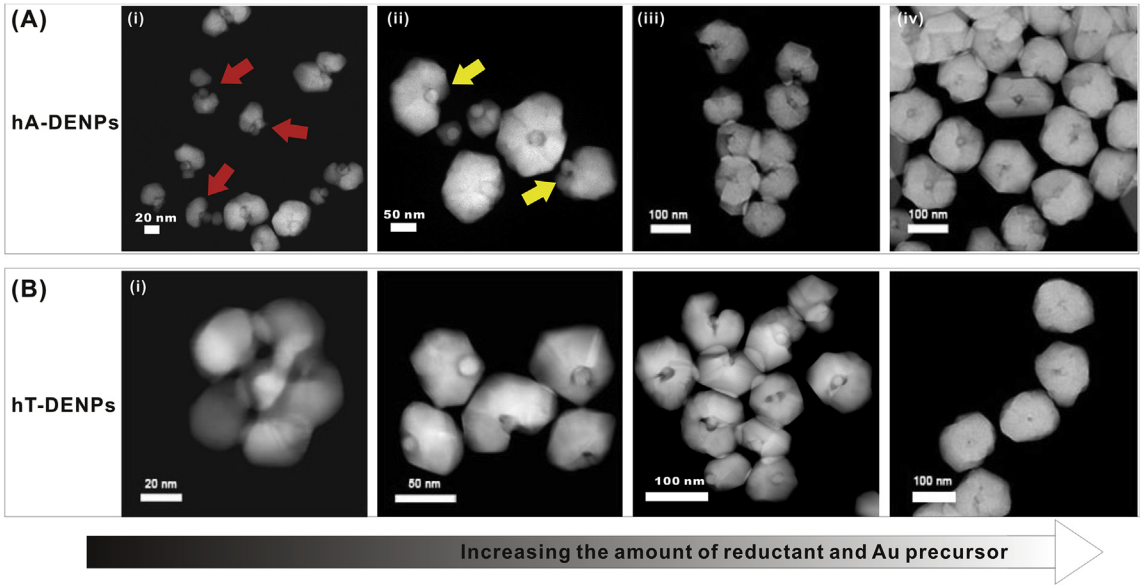

Fig. 2. HAADF-STEM images of hA-DENPs (A) and hT-DENPs (B) in four stages of preparation. Red arrow: budding structures; Yellow arrow: half-shell structures. (For interpretation of the references to colour in this figure legend, the reader is referred to the Web version of this article.)

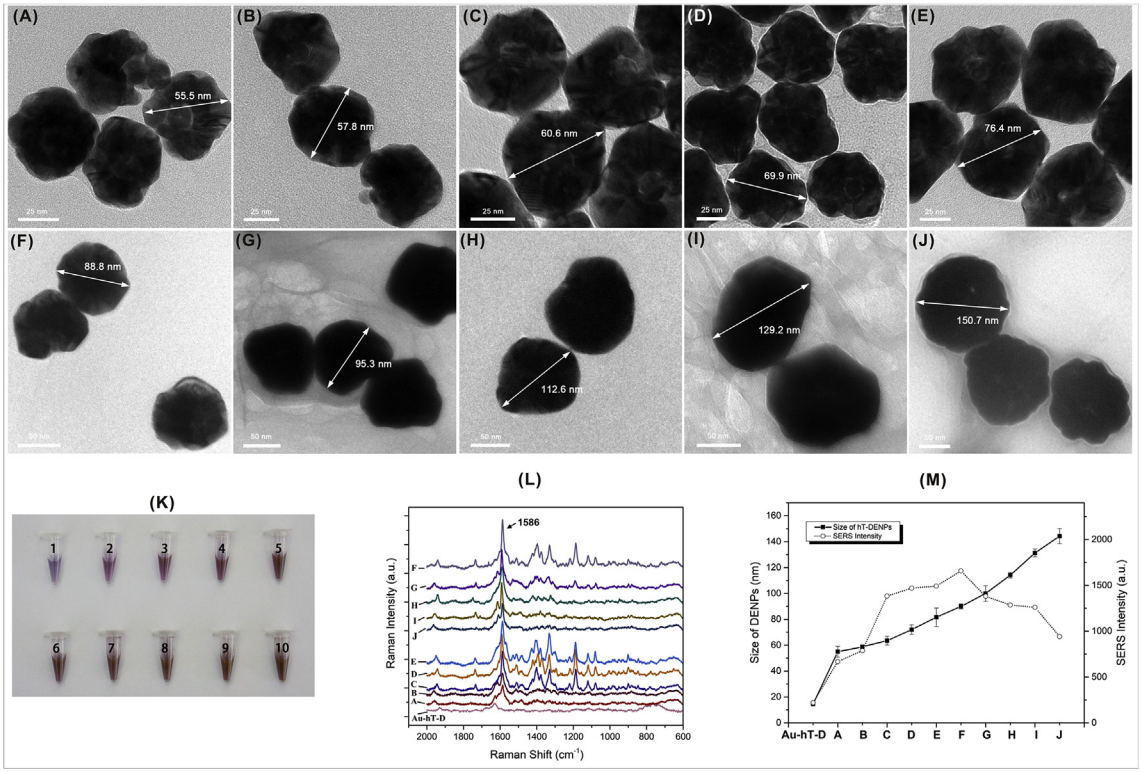

Fig. 3. (A) HAADF-STEM images of hA-DENPs synthesized with TdT elongation duration ranging between 0 min ~ 16 h for Au-hA-D cores. (B) Correlation between TdT amplification time, nanogap size, and SERS intensity. SERS spectra of hA-DENPs (C) and hT-DENPs (D), respectively. All spectra were acquired using a 633 nm excitation laser, at 2 mW, with the same particle concentration (1 nM). Laser λ = 633 nm, acquisition time; 10 s, and objective; 20×.

D. In the Synthesis of Au shell, we found that the nanogap size of the synthesized core-shell structure was different from the previously reported ~1 nm, probably resulting from the effect of hn-D strands. We systematically tuned the length of hA-D strands by varying the elongation time from 5 min to 16 h to verify whether this would provide modulation of nanogap size. The results of electrophoresis, shown in the Fig. S2, indicate that the molecular weight of products increased with elongation time. In practice, we obtained average nanogap sizes of 1.28 nm (0 min), 2.15 nm (5 min), 2.18 nm (15 min), 2.72 nm (45 min), 3.21 nm (1 h), 3.53 nm (2 h), 4.19 nm (4 h), 4.24 nm (6 h), and 5.26 nm (12 h), and 5.14 nm (16 h) (Fig. 3A), depending on the time permitted for elongation. Each average value was obtained by measuring over 50 hA-DENPs nanoparticles. The results showed that the longer the elongation time, the longer hA-D chains length, and the larger of the resulting nanogap size (Fig. 3B). There is a positive correlation between DNA chain length and nanogap size until the elongation process plateaus. Previously, DNA length was thought to pay a less significant role in controlling the size of the interior nanogap. Here, when the length of DNA embedded in core-shell structure increases dramatically, different thickness of DNA may be formed. Considering that loosely hn-D chains may prefer to lie flat and in contact with Au surface, it can be inferred that after the TdT elongation, layers of hn-D deposit on the Au surface forming a certain thickness. When Au^{3+} ions in solution are readily reduced to neutral Au atoms, they subsequently transport through hn-D layers and precipitate to form Au shell. The different thickness of the hn-D layers may affect the advance of the Au atoms to the surface of AuNP and probably form nanogaps varied in the size. Further mechanistic studies to understand the role of the hn-D strands in the formation of nanogaps are now in progress.

3.4. Tunable-nanogap and SERS signals

It is now well accepted that hot spots at the nanogap junction between particles induce enormous electromagnetic field enhancement that allows strong SERS signals to develop (Lim et al., 2011). In the work, aqueous Raman samples consisting of hA-DENPs that were excited with a 633 nm laser, presented better SERS enhancement as the TdT amplification time lengthened (Fig. S3). As shown in Fig. 3C, the characteristic Raman bands of hA-D can be easily resolved in the SERS spectrum of hA-DENPs. Among the characteristic peaks for adenine (612, 737, 1049, 1322, and 1508 cm^{-1}), the relative band intensities of the vibrations at 1322 cm^{-1} (ring stretching) and 737 cm^{-1} (ring breathing) were two strongest. A comparison of the published results clearly shows that, the adenine SERS spectra were slightly different because the orientation of DNA and other various experimental parameters may lead to changes in the SERS spectra (Barhoumi et al., 2008; Garcia-Rico et al., 2018; Morla-Folch et al., 2016; Xu et al., 2015). The SERS signal intensity at 737 cm^{-1} was chosen as the representative signal for the subsequent comparison. And it was found that the strongest SERS signals were obtained for the 5.14 nm nanogap with 16 h of amplification time (Fig. 3B). Considering that the hA-D strand itself was used as a Raman reporter, it is reasonable that the SERS signal with the greatest TdT amplification has the maximal signal. Furthermore, as shown in Fig. S4A, the time-course for peak Raman signals from hA-DENPs is highly reproducible and uniform from point to point. Although the spectral features of the DNA itself are unimportant and often are not even observable in methods utilising SERS labels previously, intense and robust SERS signals could be reproducibly obtained from the hA-DENPs in our work, which might be due to the large accumulation of bases in the nanogap after TdT elongation. In addition, in the case of hT-DENPs, we obtained spectra of nearly uniform intensity (Fig. S4B). The characteristic spectra of hT-DENPs (1062, 1187, 1320, 1396, 1477, 1586, and 1769 cm^{-1}) are shown in Fig. 3D. Control experiments were performed to illustrate conditions for plasmonic enhancement. As shown in Fig. S5, negative control groups (without Au shell, without TdT amplification) all showed negligible Raman signals.

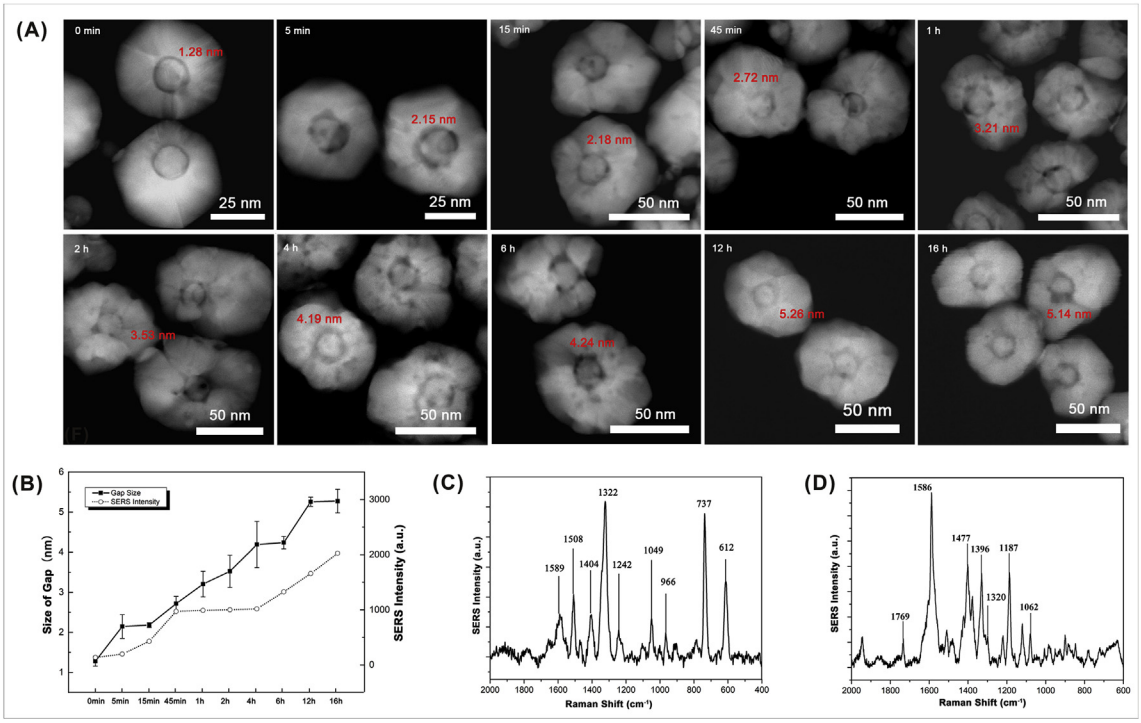

Fig. 4. TEM images of hT-DENPs in different sizes (A–J); changes in the NP colour with the increase of NP sizes (K); corresponding Raman spectra of experimental NPs (L); SERS intensity at the 1586 cm^{-1} peak based on increasing sizes of NPs under a laser wavelength of 633 nm, laser power 2 mW; acquisition time; 10 s, and objective; 20×. Error bars represent the standard deviation of three independent measurements. (For interpretation of the references to colour in this figure legend, the reader is referred to the Web version of this article.)

Since thymine has the weakest adsorption to Au among all the DNA bases and therefore should lead to the smallest nanogap, we used hT-DENPs in the subsequent experiments in combination with the above amplification optimization conditions to produce core-shell NPs for capture experiments.

3.5. Au shell thickness and SERS performance

As core-shell nanoparticles were reported to provide richer plasmonic modes owing to their size-dependent plasmonic resonances (Hu et al., 2016), we further deliberately synthesized hT-DNEPs with different shell thicknesses. In the work, Au shells of different thickness were formed on the surface of the Au-hT-D seed depending on the amount of $HAuCl_4$ added in the latter stage of synthesis. As shown in Fig. 4K, the colour of the particle solution changed from pale red (55.5 nm) to dark red (150 nm), the colour deepening gradually with the increase of nanoparticle diameter (Fig. 4A–J). The corresponding UV-vis absorption results are shown in Fig. S6. Using excitation of the 633 nm laser, we observed that hT-DENPs with different overall particle diameters exhibited SERS signals of changing amplitudes (Fig. 4L). We followed the characteristic peak at 1586 cm^{-1} for base T samples and found that the SERS peak increased with NP size, until it reached a threshold diameter (88.8 nm) (Fig. 4M). The mechanism of size-dependent Raman enhancement for metal core-shell nanoparticles has been explained in previous literatures (Guo et al., 2015; Prodan et al., 2003). The as-prepared hT-DENPs (88.8 nm) were selected and functionalized for use as target probes of bacterial capture.

3.6. hT-DENPs functionalization and bacterial Raman imaging

E. coli O157:H7 is one of the major foodborne pathogenic bacteria that often results in such serious diseases as hemolytic uremic syndrome, bloody diarrhea and even death (Ren et al., 2019; Wu et al., 2015; Zheng et al., 2019). Since it was first used for bacteria detection, SERS have attracted a great amount of attention for use in the research area of detection and identification of pathogenic microorganisms. However, the complex but similar chemical composition of bacteria makes it difficult to identify bacterial species (or strains) by their own specific Raman spectroscopic signatures. To aid in species identification, as well as to collect target species in the vicinity of the SERS probe, we functionalized hT-DENPs with an anti-*E. coli* O157:H7 antibody. We refer to these bacterial probes as hT-D-embedded core-shell SERS tags (hT-DETs). As shown in Fig. S7, the change of location of the red bands corresponding to the colour of hT-DENPs indicated successful surface functionalization. After the preparation of hT-DETs, we sought to evaluate the capture capability of the SERS tags for the *E. coli* O157:H7 bacteria by scanning electron microscopy (SEM) and Energy Dispersive X-ray Spectroscopy (EDS). SEM images of *E. coli* O157:H7 (Fig. S8A), hT-DETs (Fig. S8B), hT-DENPs incubated with *E. coli* O157:H7 (Fig. S8C) and hT-DETs incubated with *E. coli* O157:H7 (Fig. S8D) showed that hT-DETs avidly bind to *E. coli* O157:H7, while the core-shell NPs lacking antibody do not. This is confirmed further by the elemental composition from EDS data (Figs. S8E–F). Those results showed the antibody assembled on the surface of hT-DENPs had good bioactivity of *E. coli* O157:H7 recognition. To demonstrate the capture specificity, we mixed *E. coli* O157:H7 and *Staphylococcus aureus (S. aureus)* cells with hT-DETs and incubated them for 1 h. As shown in Fig. 5A, target bacteria (*E. coli* O157:H7, white arrow) showed widespread binding of hT-DETs particles (black arrow) on their surfaces, while non-targeted bacteria (*S. aureus,* yellow arrow) exhibited no bound nanoparticles. Those data clearly show good specificity and efficient targeting capability of hT-DETs.

Furthermore, we investigated the capability of hT-DETs to provide Raman signal detection. An optical microscope image of bacteria (1×10^3 CFU/mL) (Fig. S9A, white arrows) and the corresponding SERS mapping image (Fig. 5B) are shown in the same field of view. The brightness of each image was the result of hT-DETs binding to *E. coli* O157:H7 surfaces. They accurately correlate with the average SERS

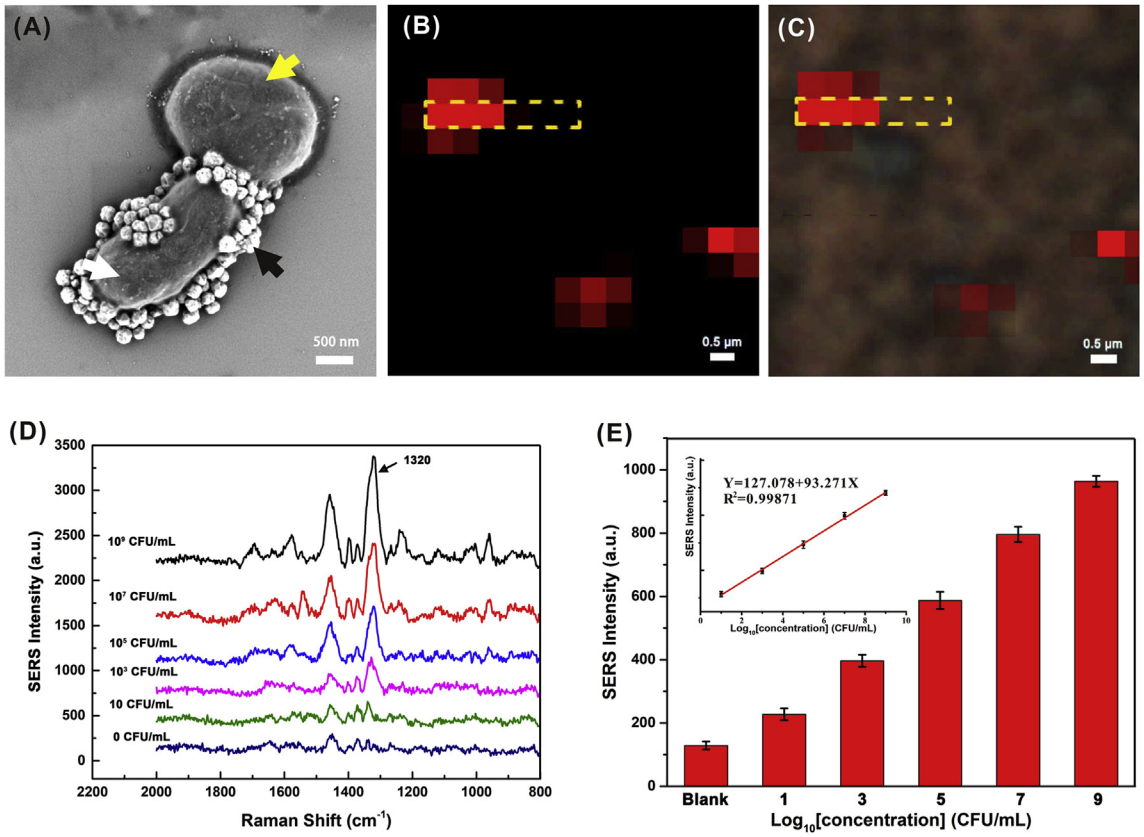

Fig. 5. (A) SEM image of hT-DETs incubated with *E. coli* O157:H7 and *S. aureus*. yellow arrow: *S. aureus*; black arrow: hT-DETs; white arrow: *E. coli* O157:H7. (B) Raman mapping image of hT-DETs distributed on *E. coli* O157:H7 cell surface under the characteristic peaks (1586 cm^{-1} for hT-D). Laser λ = 633 nm, laser power = 1 mW, acquisition time = 3 s, step size = 0.5 μm. (C) Overlay image of optical image and Raman mapping image. (D) SERS spectra acquired with different concentrations of *E. coli* O157:H7, 0, 10, 10^3, 10^5, 10^7 and 10^9 CFU/mL, respectively. (E) Concentration dependent SERS intensity of the band at 1320 cm^{-1} of hT-DETs. Insert: Calibration curve for the series concentrations of the *E. coli* O157:H7 standard solutions with six parallel experiments. The regression equation is Y = 127.078 + 93.271X with a correlation coefficient of 0.9987. Error bars represent the standard deviation of three parallel independent measurements. (For interpretation of the references to colour in this figure legend, the reader is referred to the Web version of this article.)

intensity obtained from the SERS mapping images (Raman peak at 1586 cm^{-1}) to within a 0.5 μm step size. The merged images shown in Fig. 5C illustrates that the positions of the Raman peak signal are consistent with the distribution of *E. coli* cells in the field of view. Moreover, it can be seen from Fig. S9B that the spectra from overlapping areas (yellow dotted-line box, Fig. 5C) exhibit a very good signal-to-noise ratio, which was clearly confirmed by the accurate results of S/N ratio (45.95) shown in Fig. S9C.

3.7. The limit detection of *E. coli O157:H7* and application in real food sample

The hT-DETs-based SERS assay was utilized to detect a series of *E. coli O157:H7* solution with different concentrations ranging from 0 CFU/mL to 10^9 CFU/mL. Fig. 5D shows that the SERS signal intensity gradually improved with the increasing concentration of *E. coli O157:H7*. The SERS intensity of hT-D at the band of 1320 cm^{-1} was chosen for the quantitative analysis of *E. coli* O157:H7 (Fig. 5E) and it showed a good linear relationship with the *E. coli* O157:H7 concentration (Y = 127.078 + 93.271X, R^2 = 0.9987) (Insert, Fig. 5E). Statistical analysis revealed that the detection limit of *E. coli* O157:H7 is equal to 2 CFU/mL, as estimated by using the mean (blank) +3SD. Finally, the reliability of the hT-DENPs-based SERS assay was further evaluated by recovery experiment. Different concentrations of *E. coli* O157:H7 were spiked into the blank fruit juice samples (Detailed materials can be found in Supporting Information) and then measured by SERS. As shown in Table S3, with the increase of *E. coli* O157:H7 concentration, the average recoveries of analytes were between 98.1% and 105.2%, which indicated that the hT-DETs-based SERS assay can be applied for the detection of *E. coli* O157:H7 in authentic samples.

4. Conclusions

In summary, we succeeded in synthesizing novel SERS nanoprobes based on TdT-catalyzed long single strands of DNA. Compared with the conventional SERS tags, the hn-D stands using as Raman reporters can prevent separate Raman molecules to leach out from the metal surface and eliminate the space competitive brought by additional Raman molecules. In addition, hn-D-based synthesis method overcomes the problems of conventional short polybase-mediated assembly and growth of core-shell PMNs that cannot lead to tunable nanogaps. We use optimized hT-DETs (88.8 nm) to construct the sensing assay for specific imaging and sensitive detection of *E. coli* O157:H7. The LOD for *E. coli* O157:H7 decreases to 2 CFU/mL and the average recovery of real food samples is between 98.1% and 105.2%. All these results indicate that the hn-DNEPs-based SERS assay possess better performance as a novel biosensor with good specificity and high sensitivity. We expect this method would provide a novel approach to synthesize core-shell PMNs and become a promising tool for detecting other pathogens that cause general concern in food safety and environmental monitoring.

Declaration of interest statement

The authors declare no conflict of interest.

CRediT authorship contribution statement

Yangyang Zhou: Conceptualization, Investigation, Writing - original draft. **Weina Fang:** Methodology, Writing - original draft. **Keqiang Lai:** Data curation, Investigation. **Yongheng Zhu:** Data curation, Investigation. **Xiaojun Bian:** Visualization. **Jianlei Shen:** Data curation. **Qian Li:** Validation. **Lihua Wang:** Investigation. **Weijia Zhang:** Supervision. **Juan Yan:** Writing - review & editing, Supervision.

Acknowledgements

This work was financially supported by the National Natural Science Foundation of China (21775102, 81772007, 21734003), National Key R&D Program of China (SQ2018YFC100231, 2016YFA0201200, 2016YFA0400900) and Science and Technology Commission of Shanghai Municipality (17JC1400200 and 16391903900). Innovation Program of Shanghai Municipal Education Commission (2017-01-07-00-07-E00027).

Appendix A. Supplementary data

Supplementary data to this article can be found online at https://doi.org/10.1016/j.bios.2019.111419.

References

Al-Shalalfeh, M.M., Saleh, T.A., Al-Saadi, A.A., 2016. RSC Adv. 6, 75282–75292.
Alaqad, K., Saleh, T.A., 2016. J. Environ. Anal. Toxicol. 6, 384.
Barhoumi, A., Zhang, D., Tam, F., Halas, N.J., 2008. J. Am. Chem. Soc. 130, 5523–5529.
Deng, S., Yan, J., Wang, F., Su, Y., Zhang, X., Li, Q., Liu, G., Fan, C., Pei, H., Wan, Y., 2019. Biosens. Bioelectron. 137, 263–270.
Fleischmann, M., Hendra, P.J., McQuillan, A.J., 1974. Chem. Phys. Lett. 26, 163–166.
Garcia-Rico, E., Alvarez-Puebla, R.A., Guerrini, L., 2018. Chem. Soc. Rev. 47, 4909–4923.
Graham, D., Moskovits, M., Tian, Z.Q., 2017. Chem. Soc. Rev. 46, 3864–3865.
Granger, J.H., Schlotter, N.E., Crawford, A.C., Porter, M.D., 2016. Chem. Soc. Rev. 45, 3865–3882.
Guerrini, L., Graham, D., 2012. Chem. Soc. Rev. 41, 7085–7107.
Guo, P., Sikdar, D., Huang, X., Si, K.J., Xiong, W., Gong, S., Yap, L.W., Premaratne, M., Cheng, W., 2015. Nanoscale 7, 2862–2868.
Harper, M.M., McKeating, K.S., Faulds, K., 2013. Phys. Chem. Chem. Phys. 15, 5312–5328.
Hu, C., Shen, J., Yan, J., Zhong, J., Qin, W., Liu, R., Aldalbahi, A., Zuo, X., Song, S., Fan, C., He, D., 2016. Nanoscale 8, 2090–2096.
Kang, J.W., So, P.T., Dasari, R.R., Lim, D.K., 2015. Nano Lett. 15, 1766–1772.
Khlebtsov, B.N., Khlebtsov, N.G., 2016. J. Phys. Chem. C 120, 15385–15394.
Kneipp, J., Kneipp, H., Kneipp, K., 2008. Chem. Soc. Rev. 37, 1052–1060.
Kumar, A., Kim, S., Nam, J.M., 2016. J. Am. Chem. Soc. 138, 14509–14525.
Laing, S., Gracie, K., Faulds, K., 2016. Chem. Soc. Rev. 45, 1901–1918.
Lee, J.-H., Kim, G.-H., Nam, J.-M., 2012. J. Am. Chem. Soc. 134, 5456–5459.
Lee, J.H., Oh, J.W., Nam, S.H., Cha, Y.S., Kim, G.H., Rhim, W.K., Kim, N.H., Kim, J., Han, S.W., Suh, Y.D., Nam, J.M., 2016. Small 12, 4726–4734.
Li, J.F., Zhang, Y.J., Ding, S.Y., Panneerselvam, R., Tian, Z.Q., 2017. Chem. Rev. 117, 5002–5069.
Lim, D.-K., Jeon, K.-S., Kim, H.M., Nam, J.-M., Suh, Y.D., 2010. Nat. Mater. 9, 60–67.
Lim, D.K., Jeon, K.S., Hwang, J.H., Kim, H., Kwon, S., Suh, Y.D., Nam, J.M., 2011. Nat. Nanotechnol. 6, 452–460.
Lin, L., Liu, Z., Li, X., Gu, H., Ye, J., 2017. Nanoscale 9, 2213–2218.
Lin, L., Zhang, Q., Li, X., Qiu, M., Jiang, X., Jin, W., Gu, H., Lei, D.Y., Ye, J., 2018. ACS Nano 12, 6492–6503.
Morla-Folch, J., Alvarez-Puebla, R.A., Guerrini, L., 2016. J. Phys. Chem. Lett. 7, 3037–3041.
Nam, J.M., Oh, J.W., Lee, H., Suh, Y.D., 2016. Acc. Chem. Res. 49, 2746–2755.
Nie, S., Emory, S.R., 1997. Science 275, 1102–1106.
Oh, J.W., Lim, D.K., Kim, G.H., Suh, Y.D., Nam, J.M., 2014. J. Am. Chem. Soc. 136, 14052–14059.
Prodan, E., Radloff, C., Halas, N.J., Nordlander, P., 2003. Science 302, 419–422.
Qian, X., Peng, X.H., Ansari, D.O., Yin-Goen, Q., Chen, G.Z., Shin, D.M., Yang, L., Young, A.N., Wang, M.D., Nie, S., 2008. Nat. Biotechnol. 26, 83–90.
Ren, W., Ballou, D.R., FitzGerald, R., Irudayaraj, J., 2019. Biosens. Bioelectron. 126, 324–331.
Saleh, T.A., Al-Shalalfeh, M.M., Al-Saadi, A.A., 2016. Sci. Rep. 6, 32185.
Saleh, T.A., Al-Shalalfeh, M.M., Al-Saadi, A.A., 2018. Sensor. Actuat. B-Chem. 254, 1110–1117.
Saleh, T.A., Al-Shalalfeh, M.M., Onawole, A.T., Al-Saadi, A.A., 2017. Vib. Spectrosc. 90, 96–103.
Schlucker, S., 2014. Angew. Chem. Int. Ed. Engl. 53, 4756–4795.
Shen, J., Su, J., Yan, J., Zhao, B., Wang, D., Wang, S., Li, K., Liu, M., He, Y., Mathur, S., Fan, C., Song, S., 2015. Nano Res. 8, 731–742.
Shen, J., Xu, L., Wang, C., Pei, H., Tai, R., Song, S., Huang, Q., Fan, C., Chen, G., 2014. Angew. Chem. Int. Ed. Engl. 53, 8338–8342.
Song, J., Duan, B., Wang, C., Zhou, J., Pu, L., Fang, Z., Wang, P., Lim, T.T., Duan, H., 2014. J. Am. Chem. Soc. 136, 6838–6841.
Stiles, P.L., Dieringer, J.A., Shah, N.C., Van Duyne, R.P., 2008. Annu. Rev. Anal. Chem. 1, 601–626.
Wan, Y., Wang, P., Su, Y., Wang, L., Pan, D., Aldalbahi, A., Yang, S., Zuo, X., 2015. ACS Appl. Mater. Inter. 7, 25618–25623.
Wu, S.-Y., Hulme, J., An, S.S.A., 2015. BioChip J. 9, 173–181.
Xie, X., Pu, H., Sun, D.W., 2018. Crit. Rev. Food Sci. Nutr. 16, 2800–2813.
Xu, L.J., Lei, Z.C., Li, J., Zong, C., Yang, C.J., Ren, B., 2015. J. Am. Chem. Soc. 137, 5149–5154.
Zhang, Y., Yang, P., Habeeb Muhammed, M.A., Alsaiari, S.K., Moosa, B., Almalik, A., Kumar, A., Ringe, E., Khashab, N.M., 2017. ACS Appl. Mater. Inter. 9, 37597–37605.
Zheng, L., Cai, G., Wang, S., Liao, M., Li, Y., Lin, J., 2019. Biosens. Bioelectron. 124–125, 143–149.